Ternary clathrates Ba–Zn–Ge: phase equilibria, crystal chemistry and physical properties

2007 J. Phys.: Condens. Matter 19 216223

(http://iopscience.iop.org/0953-8984/19/21/216223)

IOP PUBLISHING JOURNAL OF PHYSICS: CONDENSED MATTER

J. Phys.: Condens. Matter **19** (2007) 216223 (26pp) doi:10.1088/0953-8984/19/21/216223

Ternary clathrates Ba–Zn–Ge: phase equilibria, crystal chemistry and physical properties

N Melnychenko-Koblyuk[1], A Grytsiv[1], L Fornasari[2,3], H Kaldarar[2], H Michor[2], F Röhrbacher[2], M Koza[4], E Royanian[1,2], E Bauer[2], P Rogl[1,7], M Rotter[1], H Schmid[1], F Marabelli[3], A Devishvili[4], M Doerr[5] and G Giester[6]

[1] Institute of Physical Chemistry, University of Vienna, A-1090 Wien, Währingerstrasse 42, Austria
[2] Institute of Solid State Physics, Vienna University of Technology, A-1040 Wien, Wiedner Hauptstrasse, 8-10, Austria
[3] Physics Department 'A Volta', Universita di Pavia, I-27100, Pavia, via Bassi, 6, Italy
[4] Institute Laue Langevin, 6 rue Jules Horowitz, 38042 Grenoble, France
[5] Institute of Solid State Physics (IFP), TU Dresden, D-01062 Dresden, Germany
[6] Institute of Mineralogy and Crystallography, University of Vienna, A-1090 Wien, Althanstrasse 14, Austria

E-mail: peter.franz.rogl@univie.ac.at

Received 27 November 2006, in final form 9 March 2007
Published 2 May 2007
Online at stacks.iop.org/JPhysCM/19/216223

Abstract

The formation, phase relations, crystal chemistry and physical properties were investigated for the solid solution $Ba_8Zn_xGe_{46-x-y}\square_y$ deriving from binary clathrate $Ba_8Ge_{43}\square_3$ with a solubility limit of 8 Zn atoms per formula unit at 800 °C (□ is a vacancy). Single-crystal x-ray data throughout the homogeneity region confirm the clathrate type I structure with cubic primitive space group type $Pm\bar{3}n$.

Temperature-dependent x-ray spectra as well as heat capacity define a low-lying, almost localized, phonon branch, whereas neutron spectroscopy indicates a phonon mode with significant correlations. The transport properties are strongly determined by the Ge/Zn ratio in the framework of the structure. Increasing Zn content drives the system towards a metal-to-insulator transition; for example, $Ba_8Zn_{2.1}Ge_{41.5}\square_{2.4}$ shows metallic behaviour at low temperatures, whilst at high temperatures semiconducting features become obvious. A model based on a gap of the electronic density of states slightly above the Fermi energy was able to explain the temperature dependences of the transport properties. The thermal conductivity exhibits a pronounced low-temperature maximum, dominated by the lattice contribution, while at higher temperatures the electronic part gains weight. Zn-rich compositions reveal attractive Seebeck coefficients approaching $-180\ \mu V\ K^{-1}$ at 700 K.

(Some figures in this article are in colour only in the electronic version)

[7] Author to whom any correspondence should be addressed.

1. Introduction

The present paper continues our systematic studies of ternary clathrate phases $Ba_8M_xGe_{46-x}$ and $Ba_6M_xGe_{25-x}$, where the M element in a double-function stabilizes the clathrate structure and is used to optimize the thermoelectric performance of the material via heavy doping. Interest was hitherto mainly devoted to the thermoelectric properties of type I clathrates $Ba_8M_xX_{46-x}$ (M is Ga, In, Cu and Ni; X is Si, Ge) whereas very limited information is available on the thermoelectric performance of clathrates stabilized by other transitional metals, such as Zn. In a recent paper [1] we have dealt with the physical properties of the homologous Cd-containing clathrate system $Ba_8Cd_xGe_{46-x-y}\square_y$ and have demonstrated that increasing Cd content drives the metallic system towards a metal-to-insulator transition.

The formation and crystal structure of type I clathrates '$Ba_8Zn_xGe_{46-x}$' have been investigated by the authors of [2, 3], who determined the structure of $Ba_8Zn_8Ge_{38}$ from single-crystal data. Reference [3] furthermore listed $Ba_8Zn_8Ge_{38}$ as the limit of the compositional range and defined two vacancies per formula unit for the composition $Ba_8Zn_4Ge_{40}\square_2$. However, no data were presented for small Zn concentrations and no link was made to the binary clathrates Ba_6Ge_{25} [4] and Ba_8Ge_{43} [5, 6]. Moreover, the physical properties of ternary Ba–Zn–Ge compounds are hitherto not available in literature. In general, cage-forming clathrates are expected to be located in a region between metals and insulators where large thermopower values are found ($S \sim 1/n$, where S is the Seebeck coefficient and n the charge carrier density). Moreover, the loosely bound electropositive elements give rise to strong scattering of heat-carrying phonons, thereby reducing substantially the lattice thermal conductivity. Both phenomena may favour a promising thermoelectric performance.

Thus the principal tasks of the present investigations are (i) to establish the extensions of single-phase clathrate regions in the ternary system Ba–Zn–Ge, (ii) to elucidate details of the crystal structure of clathrate type I, (iii) to construct the phase diagram in the Ba–Zn–Ge system at 800 °C, and to investigate the physical properties of these ternary clathrates, focusing on (iv) heat capacity and (v) optical measurements, as well as on (vi) electronic and thermal transport and (vii) neutron spectroscopy of phonons. This allows insight into the lattice dynamics of the cage-structured compounds and reveals quantitative information about the thermoelectric performance.

2. Experimental details

Alloys with nominal composition $Ba_8Zn_xGe_{46-x}$ ($x = 0, 2, 4, 6, 8$ and 10) each with a mass of 2 g were prepared by melting elemental ingots (Ba 99.9, Zn 99.99 and Ge 99.999 mass%) in sealed quartz tubes at 1000 °C for 2 h. Afterwards samples were furnace cooled to 800 °C and annealed at this temperature for 4–7 days prior to quenching in cold water. Samples with nominal composition $Ba_8Zn_8Ge_{38}$ were annealed at 700, 600, 500 and 450 °C.

Details of the various techniques of characterization of composition (light optical microscopy (LOM), electron probe microanalysis (EPMA; Ba_8Ge_{43}, $BaGe_2Zn_2$ were used as standards)), of crystal structure (x-ray powder diffraction (XPD) and single crystal studies) and of physical properties (electrical and thermal conductivity, specific heat, Seebeck coefficient and thermopower) have been described in our previous paper on Cd-containing Ge-based clathrates [1]. Optical reflectance in the medium infrared at room temperature on small samples mechanically polished using diamond powder has been measured in a Fourier transform spectrometer equipped with a microscope. Spectroscopic ellipsometry has been used to directly obtain the dielectric function in the near infrared and visible spectral region. Expansion data were measured by a miniature capacitance dilatometer [7–9] in an standard Oxford

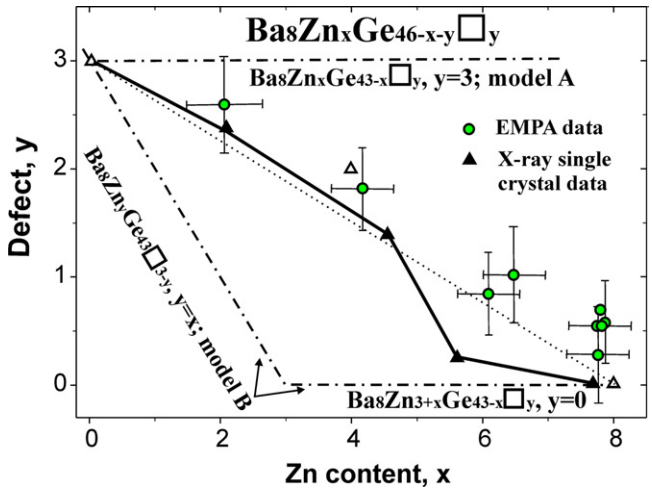

Figure 1. Dependence of defect (y) in $Ba_8Zn_xGe_{46-x-y}\square_y$ on Zn content (x). The dashed dotted lines refer to models A and B. Filled symbols—this work, open symbols— [5] for Ba_8Ge_{43} and [3] for ternary compositions.

cryomagnet equipped with a variable temperature insert. Inelastic neutron scattering (INS) data were collected at the time-of-flight spectrometer IN6 at the Institute Laue Langevin (ILL) in Grenoble, France, with an incident neutron wavelength of about 0.41 nm in the extreme time-focusing mode, offering an energy resolution of 0.15 meV in the energy range up to 10 meV. Neutron diffraction patterns were collected at 4, 50, 100 and 150 K on the D2B instrument at ILL ($\lambda_n = 0.1594$ nm; Ge (335) monochromator; collimation of 10′).

3. Results and discussion

3.1. Phase equilibria in the Ge-rich region of Ba–Zn–Ge

EPMA data on alloys $Ba_8Zn_xGe_{46-x}$ (nominal composition $x = 0$, 2, 4, 6, 8 and 10) annealed at 800 °C clearly reveal a decrease of the Ba content with increase of Zn (table 1) starting from binary $Ba_8Ge_{43}\square_3$. This result is associated with a change of the amount of vacancies in the crystal structure. Consequently, the deficiency of the structure was calculated assuming a complete Ba sublattice (Ba in 2a and 6c sites[8]). With increasing Zn content the number of voids in the lattice decreases (see figure 1) and vanishes for the composition with about 8 atoms of Zn per formula unit.

This composition simultaneously defines the solubility limit of Zn in type I clathrate at 800 °C. To elucidate the Zn incorporation in the crystal lattice of $Ba_8Ge_{43}\square_3$, the variation of the vacancy concentration versus Zn content is compared for two boundary models: *Model A* corresponds to Zn/Ge substitution at a constant level of vacancies (3 vacancies per formula as observed in binary $Ba_8Ge_{43}\square_3$). Accordingly, the resulting composition is given by the formula $Ba_8(Zn_xGe_{43-x})\square_3$. *Model B* implies that at first Zn atoms enter the three empty lattice sites and only after completely filling these sites at $x = 3$ do zinc atoms start to substitute for germanium corresponding to the formula $Ba_8(Zn_{3+x}Ge_{43-x})$. Figure 1 clearly shows that experimental data are intermediate between these two models i.e. Zn atoms fill vacancies and simultaneously substitute for Ge atoms in the framework. The vacancy concentration for

[8] Full occupancy of Ba sites was proven from single-crystal x-ray data.

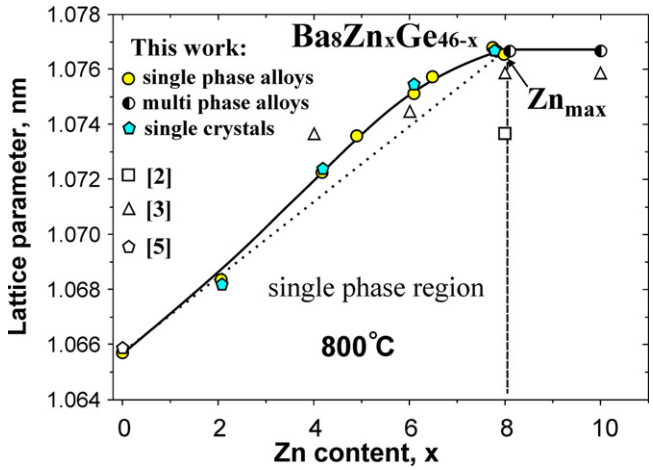

Figure 2. Composition dependence of lattice parameters (measured at room temperature) for $Ba_8Zn_xGe_{46-x}$ alloys quenched from 800 °C.

Table 1. Compositions and lattice parameters for $Ba_8Zn_xGe_{46-x-y}\square_y$.

Nominal composition	EPMA (at.%)			EPMA, formula[a]			Formula from x-ray single-crystal refinement	Lattice parameter, a (nm)
	Ba	Zn	Ge	Zn	Ge	□		
Ba_8Ge_{43}	15.7	0.0	84.3	0.0	43.0	3.0		1.065 65(2)
$Ba_8Zn_2Ge_{44}$	15.7	4.0	80.3	2.1	41.3	2.6	$Ba_8Zn_{2.1}Ge_{41.5}\square_{2.4}$	1.068 35(1)
$Ba_8Zn_4Ge_{42}$	15.4	8.0	76.6	4.2	40.0	1.8	$Ba_8Zn_{4.6}Ge_{40.0}\square_{1.4}$	1.072 26(2)
$Ba_8Zn_6Ge_{40}$	15.1	11.5	73.4	6.1	39.1	0.8	$Ba_8Zn_{5.7}Ge_{40.0}\square_{0.3}$	1.075 12(2)
$Ba_8Zn_6Ge_{40}$	15.2	12.3	72.6	6.5	38.5	1.0		1.075 73(2)
$Ba_8Zn_8Ge_{38}$	15.0	14.5	70.5	7.7	37.7	0.6		1.077 80(2)
$Ba_8Zn_8Ge_{38}$	14.9	14.5	70.6	7.8	38.0	0.3	$Ba_8Zn_{7.7}Ge_{38.3}$	1.076 47(3)
$Ba_8Zn_8Ge_{38}$	15.0	14.7	70.3	7.8	37.5	0.7		1.076 65(3)
$Ba_8Zn_8Ge_{38}$	15.0	14.7	70.3	7.8	37.6	0.5		1.076 68(3)

[a] Full occupancy of Ba sites was proven from single-crystal x-ray data.

$Ba_8Zn_xGe_{46-x-y}\square_y$ decreases with Zn content and shows some deviation from the relation $y = 3 - 3x/8$, which in this form was found to hold for the isotypic Cd-containing clathrate type I series ($Ba_8Cd_xGe_{43-5x/8}\square_{3-3x/8}(0 < x < 8)$). As a consequence of the vanishing vacancy content as well as of the slightly larger atom radius of Zn with respect to Ge, the unit cell parameters rise with the zinc content (see figure 2) showing a small positive deviation from linearity. Comparison with available literature data [2, 3] is, however, rather poor. For the nominal composition $Ba_8Zn_8Ge_{38}$ a single-phase clathrate was obtained with lattice parameter $a = 1.077\,80(2)$ nm. Ternary alloys with higher Zn content were found to be multiphase, although with a similar lattice parameter for the clathrate phase. Thus the solubility limit at 800 °C corresponds to the composition $Ba_8Zn_{8.1}Ge_{37.7}$ ($a = 1.077\,83(2)$ nm).

With respect to the limited stability range of Ba_8Ge_{43} within 770 to 810 °C [6], the long-time thermal stability of the clathrate phase at low temperature was tested on a sample with nominal composition $Ba_8Zn_8Ge_{38}$, annealed for a total of 6 months (10 days at 700 °C, 10 days at 600 °C, 150 days at 500 °C and 30 days at 450 °C with XPD at intermediate stages). For all temperatures the single-phase clathrate structure with almost identical lattice parameters was retained.

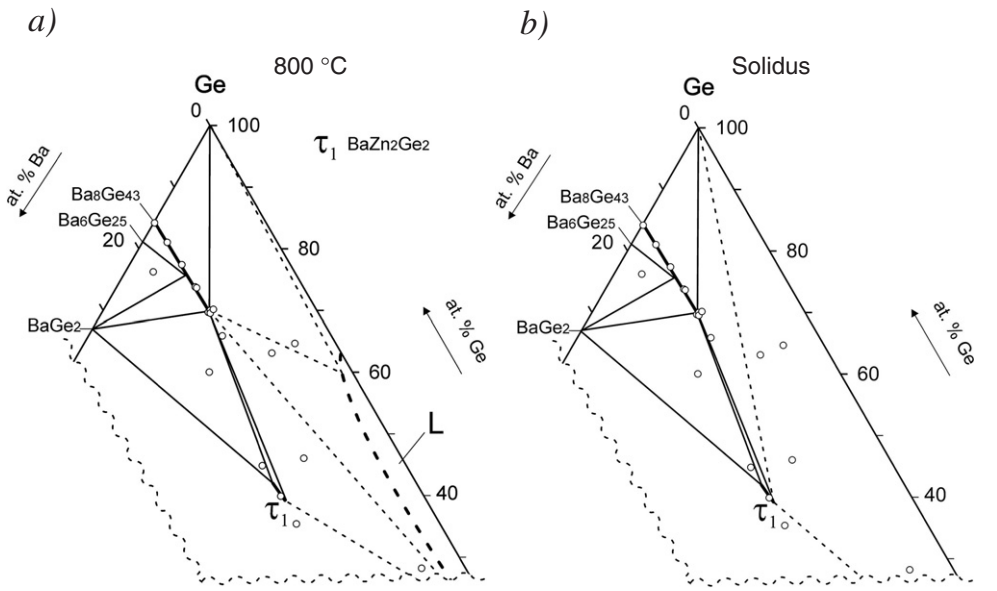

Figure 3. Isothermal 800 °C section (a) and solidus (b) of Ba–Zn–Ge ternary system in the region Zn–Ge–$BaGe_2$.

Alloys containing moisture-sensitive $BaGe_2$ quickly decompose, causing significant difficulties in specimen preparation (EPMA and LOM) resulting in complicated x-ray powder diffraction profiles due to the formation of various hydrolysis products of $BaGe_2$. In order to define the vertices of the three-phase equilibrium, clathrate I + clathrate IX + $BaGe_2$, the decomposed alloy $Ba_6Zn_2Ge_{23}$ was washed in diluted H_2SO_4 from decomposition products (brown powder) finally yielding a metallic powder which from XPD proved to be a mixture of type I and type IX clathrates. The lattice parameter for clathrate IX ($a = 1.453\,73(3)$ nm) is close to the value for binary Ba_8Ge_{25} ($a = 1.455\,63(3)$ nm from our data and $a = 1.455\,64(2)$ nm after [4]) indicating the absence of a ternary homogeneity region. The lattice parameter for clathrate type I, $a = 1.073\,52(2)$ nm, allows us to define the vertex of the three-phase equilibrium at the clathrate I solution to be at $x = 5.5$ Zn per formula unit (see figures 2 and 3).

The ternary clathrate type I forms a two-phase equilibrium to a novel ternary compound $BaZn_2Ge_2$ ($BaAl_4$ derivative structure, subcell parameters: $a = 0.451\,21(1)$ to $0.453\,69(2)$, $c = 1.0666(5)$ to $1.0563(1)$ nm). EPMA data indicate a small homogeneity region of 2.5 at.% for $Ba(Zn, Ge)_4$ at 800 °C. Details of the crystal structure and its physical properties are the subject of a forthcoming publication.

Experimental data (EPMA, XPD) on the alloys in the as-cast condition as well as after annealing at 800 °C are summarized in table 2 and were used to define the phase relations in the isothermal section in figure 3(a) as well as for a subsolidus diagram of the system in figure 3(b). At 800 °C some alloys are in equilibrium with a Zn-rich liquid (figure 3(a)).

The microstructure of sample $Ba_6Zn_{30}Ge_{64}$ annealed at 800 °C for 5 days (figure 4) clearly shows that the sample was in a solid–liquid state. The big grains of the clathrate phase with composition $Ba_8Zn_{7.9}Ge_{38.1}$ formed on annealing of the sample in liquid + solid equilibrium and were segregated on the bottom of the sample (figure 4(a)). The liquid phase decomposed on quenching of the specimen with joint crystallization of $BaZn_2Ge_2$ + (Ge), whilst the last

Table 2. EPMA and crystallographic data for selected Ba–Zn–Ge alloys annealed at 800 °C.

Nominal composition	Phase	Structure type	Lattice parameters (nm)		EPMA (at.%)		
			a	*c*	Ba	Zn	Ge
$Ba_{19.4}Zn_{6.5}Ge_{74.2}$[a]	κ_I[b], $x = 5.7$	K_4Ge_{23-x}	1.073 58(2)				
	Ba_6Ge_{25}	Ba_6Ge_{25}	1.451 52(8)				
	$BaGe_2$	$BaSi_2$					
$Ba_{20}Zn_{20}Ge_{60}$[a]	κ_I[b], $x \approx 8$	K_4Ge_{23-x}	1.076 82(3)				
	$BaZn_2Ge_2$	'$BaAl_4$'	0.453 30(6)	1.055 6(2)			
	$BaGe_2$	$BaSi_2$					
$Ba_{10}Zn_{27}Ge_{63}$	κ_I[b], $x = 7.9$	K_4Ge_{23-x}	1.077 08(2)		15.0	14.9	70.2
	eutectic				1.7	38.4	59.9
$Ba_6Zn_{30}Ge_{64}$	κ_I[b], $x = 7.9$	K_4Ge_{23-x}	1.076 26(1)		15.0	14.9	70.1
	(Ge)	C_{diam}	0.565 57(2)		0.1	0.1	99.8
	eutectic				1.6	38.3	60.1
$Ba_{20}Zn_{35}Ge_{45}$[a]	κ_I[b], $x \approx 8$	K_4Ge_{23-x}	1.076 29(2)				
	$BaZn_2Ge_2$	'$BaAl_4$'	0.453 69(2)	1.056 29(7)			
	$BaGe_2$	$BaSi_2$					
$Ba_{14}Zn_{40}Ge_{46}$	κ_I[b], $x = 8.7$	K_4Ge_{23-x}	1.077 83(2)		14.9	15.0	70.1
	$BaZn_2Ge_2$	'$BaAl_4$'	0.453 7(3)	1.062(1)	20.1	40.5	39.4
	eutectic						
$BaZn_2Ge_2$	$BaZn_2Ge_2$	'$BaAl_4$'	0.453 90(3)	1.052 79(6)	20.5	40.0	39.5
$Ba_{20}Zn_{45}Ge_{35}$[a]	$BaZn_2Ge_2$	'$BaAl_4$'	0.451 21(1)	1.066 6(5)	20.6	41.0	38.4
	$BaGe_2$	$BaSi_2$					
$Ba_6Zn_{65}Ge_{29}$	κ_I[b], $x = 8.06$	K_4Ge_{23-x}	1.076 65(2)		15.0	15.1	69.9
	$BaZn_2Ge_2$	'$BaAl_4$'	0.452 9(1)	1.057 15(8)	20.0	39.5	40.5
	eutectic				2.3	75.9	21.8

[a] The alloy was decomposed; x-ray data are from specimen powder washed in diluted H_2SO_4.
[b] κ_I—clathrate type I ($Ba_8Zn_xGe_{46-x-y}\square_y$).

portion of the liquid disappeared in a Zn-rich eutectic. This solidification behaviour allowed us to define a further reaction isotherm below 800 °C: $L + \kappa_I = BaZn_2Ge_2 + (Ge)$.

Crystallization of this clathrate from liquid led to the formation of large single-crystal specimens, which were subsequently used for measurement of physical properties. X-ray inspection of the crystal specimens on an AXS-GADDS texture goniometer ensured good quality of the diffraction spots; identical orientation matrices at various places along the sample (total length 2 cm) confirm a single-crystal condition.

3.2. Crystal chemistry of $Ba_8Zn_xGe_{46-x-y}\square_y$

Atom site preferences in $Ba_8Zn_xGe_{46-x-y}\square_y$ were derived from x-ray diffraction data collected at room temperature from single crystals at $x = 2.1$, 4.2, 6.1 and 7.8 (after EPMA). In all cases extinctions corresponded to a primitive cubic lattice (space group $Pm\bar{3}n$, $a \approx 1.1$ nm) consistent with the structure of type I clathrate. The crystal specimens investigated did not exhibit any extra reflections for a larger unit cell $a' = 2a$ as reported by [6] for binary $Ba_8Ge_{43}\square_3$.

The barium atoms as heavy x-ray scatterers were unambiguously found at the sites 2a (0, 0, 0) and 6c (1/4, 0, 1/2). In refinement of the single-crystal intensity data we were unable to distinguish between Zn and Ge atoms due to the close x-ray scattering power of these elements. Employing neutron diffraction with a significant difference of scattering lengths of

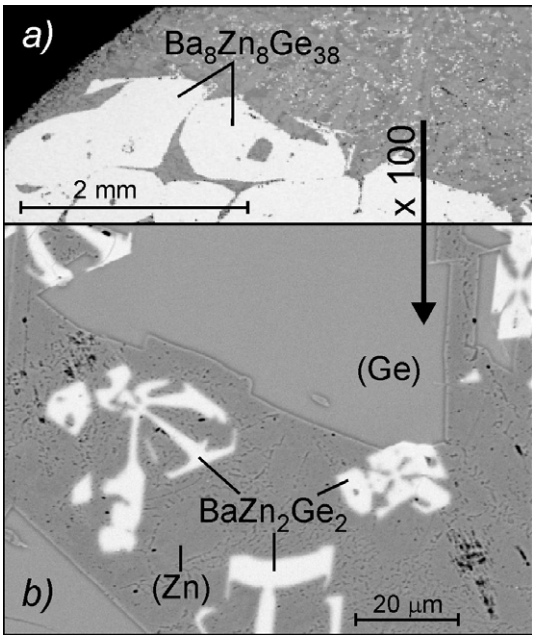

Figure 4. Microstructures of $Ba_6Zn_{30}Ge_{64}$ annealed at 800 °C.

Zn and Ge atoms ($b_{Zn} = 5.680$ fm and $b_{Ge} = 8.185$ fm), the Zn atoms in $Ba_8Zn_{7.7}Ge_{38.3}$ were unambiguously found to completely occupy the 6d site and partially substitute for Ge in the 16i site (0.1Zn + 0.9Ge, $x = 0.183\,55(5)$, $R = 0.024$, 4 K). Thus the atom site distribution for $Ba_8Zn_xGe_{46-x-y}\square_y$ corresponds to the Cd-homologue series, $Ba_8Cd_xGe_{43-5x/8}\square_{3-3x/8}$ [1]: at low Zn content the 6d site contains Ge atoms, Zn atoms and vacancies, the latter decreasing with rising Zn content. This decrease of the vacancy level was confirmed by Rietveld refinements (table 3) and the EPMA data. At Zn contents larger than 6 atoms per unit cell, the 6d site appears to be completely filled with Zn atoms. The remaining Zn is suggested (from similarity with $Ba_8Cd_xGe_{43-5x/8}\square_{3-3x/8}$) to occupy the 16i site (see tables 3 and 4)[9]. For all refinements anisotropic atomic displacement parameters (ADPs; U_{ij}) were employed. Refinements show that incorporation of Zn atoms into the crystal lattice does not affect the geometry of the 16i site ($x, x, x = 0.1835(2)$).

Analysing the thermal atomic displacement parameters (ADPs), we encountered a large anisotropy of electron densities in two cases: (i) Ba atoms in the 6c site for all investigated single crystals and (ii) Ge atoms in 24k site (Ge3) for Zn concentrations smaller than $x = 4.5$. However, with increasing Zn content the anisotropy of ADPs for Ge3 decreases and finally vanishes for $x > 6$. As the direction of the ADP ellipsoids point towards the nearest neighbours in the 6d site (M1), we may associate this behaviour with vacancy formation: the three species (Ge atoms or Zn atoms or vacancies) occupying the 6d site engage in different interactions with Ge3 atoms located in the 24k site and interatomic distances d_{M1-Ge3} increase in the sequence □–Ge, Ge–Ge, Zn–Ge. Accordingly the shape of the 24k site electron density adopts an ellipsoid elongated along the direction of the M–Ge3 bonds. For binary Ba_8Ge_{43}—where only Ge-atoms

[9] It should be noted that (in fine agreement with our findings on $Ba_8Zn_{7.7}Ge_{38.3}$) powder neutron diffraction on the homologous $Sr_8Zn_8Ge_{38}$ compound, exploiting the higher difference in the neutron scattering factors of $b_{Zn} = 5.7$ and $b_{Ge} = 8.4$ fm as compared to x-ray data, revealed preferred occupation of Zn atoms in the 6d site ($occ_{Zn} = 0.88$) and 16i site ($occ_{Zn} = 0.10$) [11].

Table 3. X-ray single-crystal data for $Ba_8Zn_xGe_{46-x-y}\square_y$ at $x = 2.1$, 4.2, 6.1 (room temperature, ω-scans, scan width 2°; redundancy > 10); clathrate—type I; space group $Pm\bar{3}n$, No. 223; standardized with program *Structure Tidy* [10].

	Compound[a]		
Parameter	$Ba_8Zn_2Ge_{44}$	$Ba_8Zn_4Ge_{42}$	$Ba_8Zn_6Ge_{40}$
Formula from EPMA	$Ba_8Zn_{2.1}Ge_{41.3}\square_{2.6}$	$Ba_8Zn_{4.2}Ge_{40.0}\square_{1.8}$	$Ba_8Zn_{6.1}Ge_{39.1}\square_{0.8}$
Formula from refinement	$Ba_8Zn_{2.1}Ge_{41.5}\square_{2.4}$	$Ba_8Zn_{4.6}Ge_{40.00}\square_{1.4}$	$Ba_8Zn_{5.7}Ge_{40.0}\square_{0.3}$
Crystal size	$32 \times 44 \times 50\ \mu m^3$	$50 \times 58 \times 60\ \mu m^3$	$42 \times 56 \times 50\ \mu m^3$
a (nm)	1.068 27(2)	1.072 33(2)	1.075 48(2)
a (nm), Ge standard	1.068 35(1)	1.072 26(2)	1.075 12(2)
μ_{abs} (mm^{-1})	32.37	32.39	32.53
Data collection, 2Θ range (deg)	$2 \leqslant 2\Theta \leqslant 72.6$; 100 s/frame	$2 \leqslant 2\Theta \leqslant 72.0$; 50 s/frame	$2 \leqslant 2\Theta \leqslant 72.5$; 75 s/frame
Total number of frames	208 4 sets	201 6 sets	210 5 sets
Reflections in refinement	$473 \geqslant 4\sigma(F_o)$ of 562	$474 \geqslant 4\sigma(F_o)$ of 567	$556 \geqslant 4\sigma(F_o)$ of 591
Mosaicity	<0.53	<0.45	<0.43
Number of variables	21	21	19
$R_F^2 = \Sigma\lvert F_0^2\text{-}F_c^2\rvert/\Sigma F_0^2$	0.0229	0.0221	0.020
R_{Int}	0.066	0.056	0.061
wR2	0.0539	0.0529	0.053
GOF	1.124	1.185	1.19
Extinction (Zachariasen)	0.0006(1)	0.0008(1)	0.0011(1)
Ba1 in 2a (0, 0, 0); occ.	1.00(1)	1.00(1)	1.00(1)
$U_{11} = U_{22} = U_{33}$ (in 10^2 nm^2)	0.0101(1)	0.0090(1)	0.0099(1)
Ba2 in 6c (1/4, 0, 1/2); occ.	1.00(1)	1.00(1)	1.00(1)
U_{11}; $U_{22} = U_{33}$	0.0201(3); 0.0369(2)	0.0179(2); 0.0343(2)	0.0176(2); 0.0379(2)
M1 in 6d (1/4, 1/2, 0); occ.	0.253 Ge + 0.343[b] Zn + 0.404 □	0.762 Zn + 0.238 □	0.954 Zn + 0.046 □
U_{11}; $U_{22} = U_{33}$	0.0106(6); 0.0098(4)	0.0104(5); 0.0093(4)	0.0114(4); 0.0104(3)
M2 in 16i (x, x, x); occ.	1.02(1)Ge	1.00(1)Ge	1.00(1)Ge
x:	0.183 44(2)	0.183 48(2)	0.183 69(2)
$U_{11} = U_{22} = U_{33}$; $U_{23} = U_{13} = U_{12}$	0.0117(1); −0.0019(1)	0.0098(1); −0.0015(1)	0.0089(1); −0.0010(1)

Table 3. (Continued.)

Parameter	Compound[a]								
	$Ba_8Zn_2Ge_{44}$			$Ba_8Zn_4Ge_{42}$			$Ba_8Zn_6Ge_{40}$		
Ge31 in 24k (0, y, z); occ.	0.726(3)Ge			0.873(4)Ge			0.99(1)Ge		
y, z	0.115 71(11); 0.309 98(12)			0.117 15(8); 0.310 24(9)			0.11768(3); 0.31001(3)		
U_{11}; U_{22}	0.0120(2); 0.0125(4)			0.0105(2); 0.0108(3)			0.0102(2); 0.0100(2)		
U_{33}; U_{23}	0.0136(5); 0.0003(3)			0.0109(3); 0.0001(2)			0.0106(2); 0.0001(1)		
Ge32 in 24k (0, y, z); occ.	0.274(3)Ge			0.127(4)Ge					
y, z	0.132 20(34); 0.336 85(30)			0.130 62(62); 0.337 88(59)					
U_{11}; U_{22}	0.0120(2); 0.0125(4)			0.0105(2); 0.0108(3)					
U_{33}; U_{23}	0.0136(5); 0.0003(3)			0.0109(3); 0.0001(2)					
Residual density e Å^{-3}; max; min	1.95; −1.60			2.02; −1.19			1.72; −0.88		
Principal mean-square atomic displacements U	Ba1 0.0101	0.0101	0.0101	Ba1 0.0094	0.0094	0.0094	Ba1 0.0099	0.0099	0.0099
	Ba2 0.0369	0.0369	0.0201	Ba2 0.0343	0.0343	0.0179	Ba2 0.0379	0.0379	0.0176
	M1 0.0106	0.0098	0.0098	Zn1 0.0104	0.0093	0.0093	M1 0.0114	0.0105	0.0105
	Ge2 0.0136	0.0136	0.0078	Ge2 0.0112	0.0112	0.0069	Ge2 0.0100	0.0100	0.0068
	Ge31 0.0137	0.0125	0.0120	Ge31 0.0109	0.0108	0.0105	Ge3 0.0106	0.0102	0.0100
	Ge32 0.0137	0.0125	0.0120	Ge32 0.0109	0.0108	0.0105			
	Interatomic distances, standard deviation less than 0.0003 nm								
Ba1–8M2	0.3394			0.3408			0.3422		
–12Ge31	0.3535			0.3556			0.3566		
–12Ge32	0.3866			0.3884					
Ba2–8Ge32	0.3488			0.3488					
–8Ge31	0.3575			0.3592			0.3606		
–4M1	0.3777			0.3791			0.3802		
–8M2	0.3973			0.3987			0.3998		
–4Ge32	0.4037			0.4071					
–4Ge31	0.4155			0.4156			0.4162		

Table 3. (Continued.)

Parameter	Compound[a]		
	$Ba_8Zn_2Ge_{44}$	$Ba_8Zn_4Ge_{42}$	$Ba_8Zn_6Ge_{40}$
	Interatomic distances, standard deviation less than 0.0003 nm		
M1–4Ge32	0.2150	0.2159	
–4Ge31	0.2486	0.2484	0.2490
–4Ba2	0.3777	0.3791	0.3802
M2–1M2	0.2463	0.2471	0.2471
–3Ge31	0.2488	0.2495	0.2500
–3Ge32	0.2613	0.2633	
–1Ba1	0.3394	0.3408	0.3422
Ge31–1Ge32	0.0337	0.0330	
–1Ge31	0.2472	0.2512	0.2490
–1M1	0.2486	0.2484	
–2M2	0.2488	0.2664	0.2500
–1Ge32	0.2664	0.2673	
–2Ba2	0.3575	0.3592	0.3606
–1Ba1	0.3535	0.3556	0.3566
Ge32–1Ge32	0.0337	0.0330	
–1Ge31	0.2664	0.2673	
–1M1	0.2150	0.2159	
–2M2	0.2613	0.2633	
–1Ge32	0.2825	0.2801	
–2Ba2	0.3488	0.3488	
–1Ba1	0.3866	0.3884	

[a] Nominal composition.
[b] Fixed value.

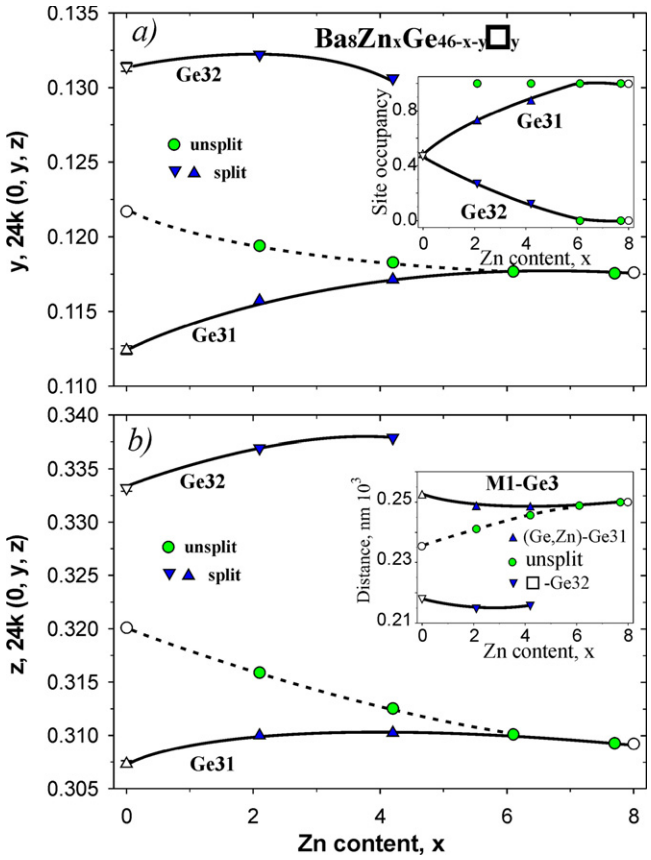

Figure 5. Compositional dependence of positional parameters y (a) and z (b) for the Ge3 site 24k $(0, y, z)$ in $Ba_8Zn_xGe_{46-x-y}\square_y$. Filled symbol—our data, open— [5] for Ba_8Ge_{43} and [2, 3] for ternary compounds.

and vacancies share the 6d site— [4–6] reported a split of the 24k site into two 24k sites (Ge31 and Ge32). This possibility was carefully checked for all crystals. Indeed in refinements for $x < 6$ using split atom positions ($occ_{Ge31} + occ_{Ge32} = 1$) the reliability factors decrease from about 4 to 2.5% and residual electron densities from 4 to less than 1.5 e Å^{-3}, yielding featureless difference-Fourier maps $F_{obs} - F_{calc}$. The results of the refinement are listed in tables 3 and 4.

Three facts have to be emphasized describing the Ge3 sites: (i) as seen from the inset in figure 5(a), the population of Ge31 rises with increasing Zn content from ∼50% in Ba_8Ge_{43} to a full occupation for $x > 6$; (ii) consequently the y and z parameters of Ge31 approach the values of the unsplit model for $x > 6$ (see figures 5(a), (b)); (iii) the internal distance $d_{Ge31-Ge32}$ stays constant for all crystals where split sites were used (see inset in figure 5(b)). The changes in the Ge3 sites correlate with changes in the 6d site: the decrease of the amount of vacancies in the 6d site with simultaneous increase of Zn content results in the disappearance of the Ge32 atoms. For almost complete occupation of the 6d site by Zn atoms, the electron density centred at site 24k finally adopts a regular shape (see tables 3 and 4).

The change of the crystallographic parameters (lattice parameter, atomic coordinates and site occupancy) with Ge/Zn substitution is well reflected by a compositional dependence of the

Table 4. X-ray single-crystal data for $Ba_8Zn_{7.7}Ge_{38.3}$ at various temperatures (ω-scans, scan width 2°; redundancy >12); clathrate—type I; space group $Pm\bar{3}n$, No. 223; standardized with program *Structure Tidy* [10].

	Temperature		
Parameter	296 K	200 K	100 K
Crystal size	40 × 54 × 70	40 × 54 × 70	40 × 54 × 70
a (nm)	1.076 78(2)	1.075 35(2)	1.074 17(2)
μ_{abs} (mm^{-1})	32.61	32.61	32.61
Data collection, 2Θ range (deg)	$2 \leqslant 2\Theta \leqslant 72.6$; 80 s/frame	$2 \leqslant 2\Theta \leqslant 72.0$; 80 s/frame	$2 \leqslant 2\Theta \leqslant 72.5$; 80 s/frame
Total number of frames	236 5 sets	236 5 sets	236 5 sets
Reflections in refinement	$493 \geqslant 4\sigma(F_o)$ of 573 [2103]	$503 \geqslant 4\sigma(F_o)$ of 568 [1936]	$515 \geqslant 4\sigma(F_o)$ of 567 [2072]
Mosaicity	<0.45	<0.46	<0.44
Number of variables	19	19	19
$R_F^2 = \Sigma\lvert F_0^2 - F_c^2\rvert / \Sigma F_0^2$	0.0205	0.0252	0.0224
R_{Int}	0.062	0.063	0.061
wR2	0.0488	0.0502	0.0500
GOF	1.078	1.283	1.181
Extinction (Zachariasen)	0.0065(2)	0.001 29(9)	0.000 88(9)
Ba1 in 2a (0, 0, 0); occ.	1.00(1)	1.00(1)	1.00(1)
$U_{11} = U_{22} = U_{33}$ (in 10^2 nm^2)	0.0116(2)	0.0083(2)	0.0059(1)
Ba2 in 6c (1/4, 0, 1/2); occ.	1.00(-)	1.00(-)	1.00(-)
U_{11}; $U_{22} = U_{33}$	0.0202(3); 0.0580(3)	0.0148(3); 0.0486(4)	0.0104(2); 0.0406(2)
Zn1 in 6d (1/4, 1/2, 0); occ.	1.02(1)	1.03(1)	1.01(1)
U_{11}; $U_{22} = U_{33}$	0.0130(4); 0.0116(3)	0.0093(4); 0.0083(3)	0.0061(3); 0.0053(2)
M2 in 16i (x, x, x); occ.[a]	0.889(2)Ge + 0.110Zn[a]	0.880(5)Ge + 0.110Zn[a]	0.887(3)Ge + 0.110Zn[a]
x:	0.183 76(2)	0.183 77(3)	0.183 72(2)
$U_{11} = U_{22} = U_{33}$; $U_{23} = U_{13} = U_{12}$	0.0103(1); −0.0010(1)	0.0069(1); −0.0008(1)	0.0050(1); −0.0005(1)

Table 4. (Continued.)

Parameter	Temperature								
	296 K			200 K			100 K		
Ge3 in 24k (0, y, z); occ.	0.987(3)			0.986(5)			0.994(3)		
y; z	0.117 56(3); 0.309 27(3)			0.117 52(4); 0.309 40(4)			0.117 47(3); 0.309 39(3)		
U_{11}; U_{22}	0.0117(2); 0.0108(2)			0.0084(2); 0.0077(2)			0.0058(1); 0.0054(1)		
U_{33}; U_{23}	0.0104(2); −0.0006(1)			0.0073(2); −0.0006(1)			0.0054(1); −0.0003(1)		
Residual density; max; min	1.18; −0.82			1.03; −1.73			1.06; −1.89		
Principal mean-square atomic displacements U	Ba1 0.0116	0.0116	0.0116	Ba1 0.0083	0.0083	0.0083	Ba1 0.0059	0.0059	0.0059
	Ba2 0.0580	0.0580	0.0202	Ba2 0.0486	0.0486	0.0148	Ba2 0.0407	0.0407	0.0104
	Zn1 0.0130	0.0116	0.0116	Zn1 0.0093	0.0083	0.0083	Zn1 0.0061	0.0053	0.0053
	M2 0.0113	0.0113	0.0082	M2 0.0077	0.0077	0.0054	M2 0.0055	0.0055	0.0041
	Ge3 0.0117	0.0112	0.0100	Ge3 0.0084	0.0081	0.0069	Ge3 0.0058	0.0057	0.0050
	Interatomic distances, standard deviation less than 0.0003 nm								
Ba1–8M2	0.3427			0.3423			0.3418		
–12Ge3	0.3563			0.3559			0.3555		
Ba2–8Ge3	0.3615			0.3609			0.3605		
–4Zn1	0.3807			0.3802			0.3798		
–8M2	0.4002			0.3997			0.3993		
–4Ge3	0.4167			0.4162			0.4158		
Zn1–4Ge3	0.2500			0.2496			0.2494		
–4Ba2	0.3807			0.3802			0.3798		
M2–3Ge3	0.2500			0.2498			0.2495		
–1M2	0.2471			0.2467			0.2466		
–1Ba1	0.3427			0.3423			0.3418		
Ge3–1Ge3	0.2532			0.2527			0.2524		
–2M2	0.2500			0.2498			0.2495		
–1Zn1	0.2500			0.2496			0.2494		
–1Ba1	0.3563			0.3559			0.3555		
–2Ba2	0.3615			0.3609			0.3605		

[a] Fixed value.

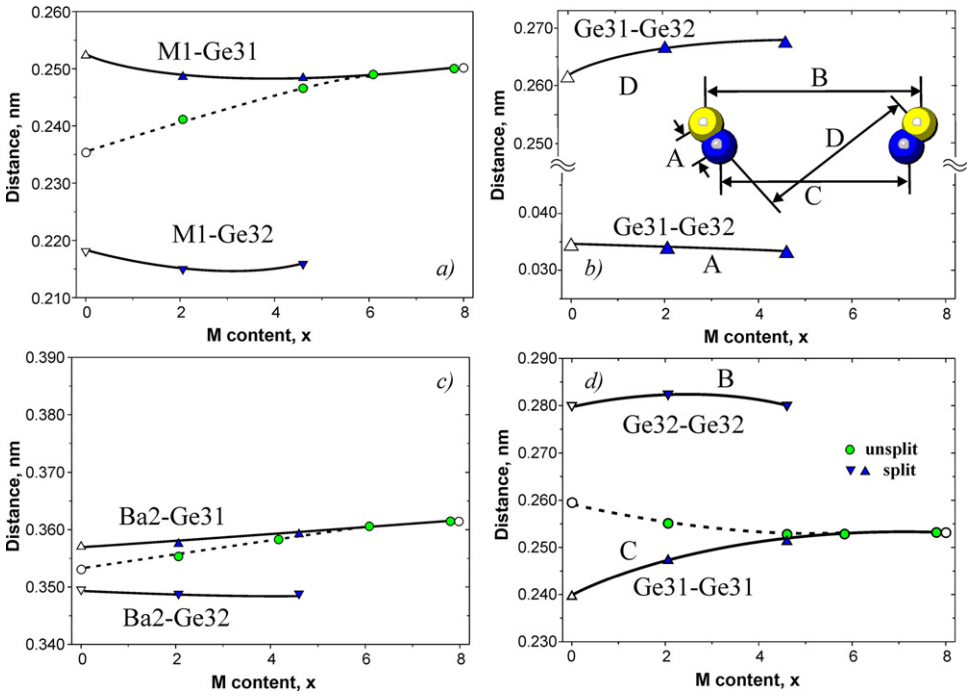

Figure 6. Selected interatomic distances for M1–Ge3 (a), Ba2–Ge3 (b) and Ge3–Ge3 (c), (d) in $Ba_8Zn_xGe_{46-x-y}\square_y$. Filled symbols—this work, open symbols—[5] for Ba_8Ge_{43} and [3] for ternary compositions.

interatomic distances (tables 3, 4 and figure 6). In further discussions we accepted the alloy compositions as derived from x-ray single-crystal refinements (table 1).

Whereas the ADPs for Ba2 atoms in the 6c site at the centres of flattened tetrakaidecahedra show a significant anisotropy (tables 3 and 4), Ba1 atoms (spherical by symmetry at the centres of almost regular pentagondodecahedra) do not show a thermal displacement factor enhanced over the general ADP values for framework atoms. Thus no special rattling effect can be derived for Ba1 atoms. It is interesting to mention here that the lighter and slightly smaller Sr1 atoms in $Sr_8Zn_8Ge_{38}$ do show an about two times higher ADP than the Ge framework [11]. If the $Ba_8Zn_{7.7}Ge_{38.3}$ crystal is considered as a simple Debye solid with Ba2 atoms behaving like Einstein oscillators, the thermal displacements and the Einstein temperatures $\Theta_{E,ii}$ are related by

$$U_{ii} = \frac{\hbar^2}{2m_{Ba}k_B\Theta_{E,ii}} \coth\left(\frac{\Theta_{E,ii}}{2T}\right),$$

where m_{Ba} is the atomic mass of Ba [12]. From the linear slope $\Delta U_{ii}/\Delta T$ in figure 7 (high-temperature approximation, where $h\nu < 2k_BT$) the force constants, K_{ii} (g s^{-1}), the frequency of vibrations, ν_{ii} [10^{12} s^{-1}], and hence the Einstein temperatures, $\Theta_{E,ii} = \frac{h\nu_{ii}}{k_B}$ (K), can be extracted. From symmetry constraints U_{11} is different from $U_{22} = U_{33}$, yielding $\Theta_{E,11} = 85$ K and $\Theta_{E,22} = 64$ K in line with the flat rotational ellipsoid of Ba2 atoms squeezed between the two hexagons of the framework tetrakaidecahedron. Although with decreasing temperature the ratio U_{22}/U_{11} for Ba2 atoms increases from 3 at 300 K to 4 at 100 K, neutron powder diffraction data at 4 K (Fourier map) show no signs of a split position at the Ba2 site.

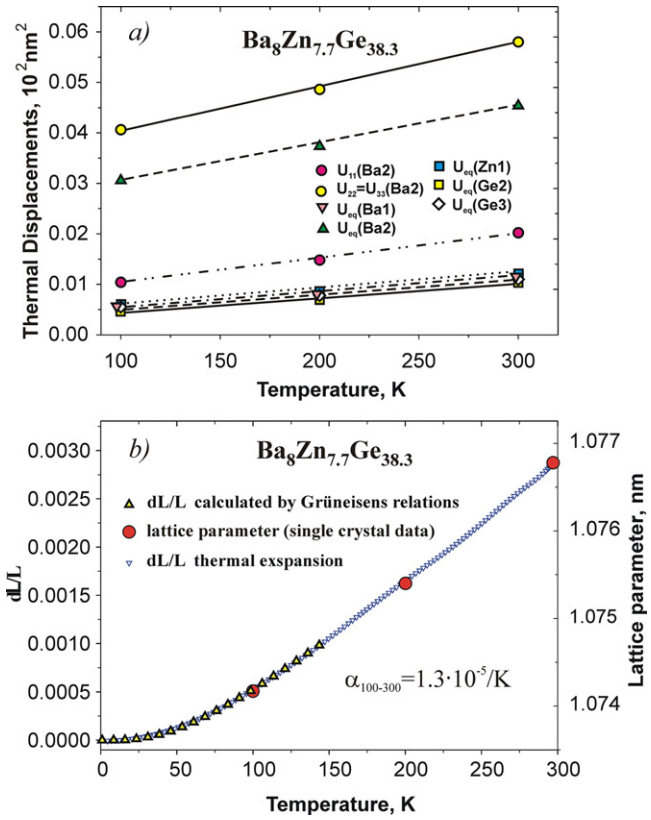

Figure 7. (a) Temperature displacement parameters and (b) thermal expansion of $Ba_8Zn_{7.7}Ge_{38.3}$ versus temperature. The small triangles refer to the thermal expansion data measured on a bulk polycrystal; the circles indicate the temperature dependence of the lattice parameter measured by x-ray diffraction on a single crystal. For comparison the calculation of the thermal expansion based on the Grüneisen relation is shown (large triangles).

The temperature dependence of the lattice parameters (measured for three temperatures (100, 200 and 296 K)) on a single-crystal specimen fits very well on the lattice expansion curve derived from capacitance measurements; see text below and figure 7. Compared to $Sr_8Zn_8Ge_{38}$ ($\alpha = 3.6 \times 10^{-5}$ K^{-1} [11]) the thermal expansion $Ba_8Zn_{7.7}Ge_{38.3}$ ($\alpha = 1.3 \times 10^{-5}$ K^{-1}) is about three times smaller and thus similar to the diamond phase of germanium. A least-squares fit of the lattice parameter expansion curve to a fourth-order polynomial allows a perfect representation of $a(T)$: a (nm) $= 1.0736 - 2.0286 \cdot T + 1.0691 \times 10^{-7} \cdot T^2 - 3.5909 \times 10^{-9} \cdot T^3 + 4.6993 \times 10^{-13} \cdot T^4$.

3.3. Physical properties

3.3.1. Temperature-dependent heat capacity. Temperature-dependent heat capacity measurements were carried out on $Ba_8Zn_{7.7}Ge_{38.3}$. The results of this investigation are displayed in figures 8(a), (b) as C_p versus T and as $(C_p - \gamma T)/T^3$ versus $\ln T$. The latter representation allows emphasizing deviations from the simple Debye model, which at low temperatures causes a T^3 dependence. Note that the Sommerfeld value $\gamma \cong 2$ mJ mol^{-1} K^{-2} is also subtracted in figure 8(b). Obviously, the heat capacity of $Ba_8Zn_{7.7}Ge_{38.3}$ exhibits

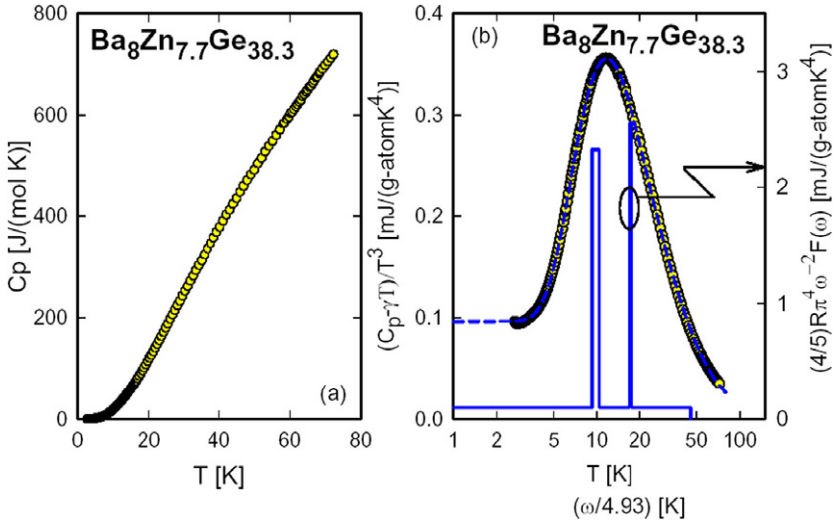

Figure 8. Temperature-dependent specific heat C_p of $Ba_8Zn_{7.7}Ge_{38.3}$, plotted as C_p versus T (a) and $(C_p - \gamma T)/T^3$ versus $\ln T$ (b). The dashed line is a least-squares fit of the experimental data using the model described in the text with two Einstein-like modes ($\Theta_D = 225$ K, $\Theta_{EL1} = 48.4$ with width of 5.6 K and $\Theta_{EL2} = 84.8$ with a width of 4 K). The dashed–double-dotted line represents an alternative fit with a single Einstein-like mode ($\Theta_D = 240$ K, $\Theta_{EL} = 62$ with width of 56 K). The solid and the dashed–dotted lines sketch the phonon spectral function $F(\omega)$ plotted as $\omega/4.93$ versus $(5/4)R\pi^4\omega^{-2}F(\omega)$ for which ω is given in kelvin.

distinct deviations from a Debye-like behaviour in the entire temperature range studied. In fact, a standard plot of the heat capacity data according to C_p/T versus T^2 does not reveal any sufficiently extended temperature range, where the simple behaviour of metals holds, i.e., $C_p/T = \gamma T + \beta T^3$. The finite value of γ refers to a finite electronic density of states at the Fermi energy, thus indicating a metallic state, at least, for $Ba_8Zn_{7.7}Ge_{38.3}$. Also, the complete Debye function is unable as well to account for the temperature-dependent specific heat of $Ba_8Zn_{7.7}Ge_{38.3}$ in an extended temperature range. Figure 8(a) also shows that there are no phase transitions below about 80 K.

Significant deviations from the simple Debye model indicate a rather complicated phonon spectrum in this family of clathrates. This spectrum is assumed to be composed of background vibrations originating from the cage-like structure (represented by a Debye spectrum) and, additionally, from the rattling modes of loosely bound electropositive Ba atoms. The latter can be accounted for in terms of Einstein frequencies. In order to qualitatively and quantitatively describe the lattice dynamics, we have adapted a model which incorporates some fine structure in the phonon density of states [13, 14]. The latter is represented by a spectral function $F(\omega)$, allowing us to express the heat capacity as

$$C_{ph}(T) = 3R \int_0^\infty F(\omega) \frac{(\frac{\omega}{2T})^2}{\sinh^2(\frac{\omega}{2T})} \, d\omega, \tag{1}$$

with ω the phonon frequency. The most common assumptions on $F(\omega)$ are $F(\omega) = \delta(\omega)$ and $F(\omega) \sim \omega^2$ up to a cut-off frequency ω_D, corresponding to the well-known Einstein and Debye model, respectively. Junod *et al* [13] demonstrated that certain functionals of the phonon specific heat take the form of convolutions of the phonon spectrum. In particular, $(5/4)R\pi^4 C_{ph}T^3$ is an image of the spectrum $\omega^{-2}F(\omega)$ for $\omega = 4.93T$, where ω is expressed in kelvin. Based on these considerations we have constructed an elementary phonon spectrum

and have carried out least-squares fits to the data. The results of this procedure are also shown in figure 8.

In a first approximation we have assumed that, besides a Debye density of states, the system is composed of two additional, energetically separated Einstein-like modes. However, in contrast to the standard Einstein model of the specific heat, a certain frequency width for each of these branches is allowed. The results of this fit are represented in figure 8 as a dashed line. The overall goodness of the fit is extremely high, revealing a Debye temperature $\Theta_{\mathrm{D}} = 225$ K and two narrow structures at $\Theta_{\mathrm{EL1}} = 48.4$ K and $\Theta_{\mathrm{EL2}} = 84.8$ K, with corresponding spectral widths of 5.6 and 4 K, respectively. Accordingly, both contributions have different spectral weights. Based on this fit, the phonon spectrum is constructed and plotted in figure 8 referring to the right axis (solid line). The spectral weight follows from the constraint that for $T \to 0$ the height of the phonon density of states coincides with the value of C_p/T^3 for $T \to 0$. It is interesting to note that a similar class of materials, i.e. skutterudites, has been found with similar widths of Einstein-like modes [15].

Similar localized lattice vibrations were also derived from our XRD analysis of the anisotropic thermal displacement factor of Ba2, yielding two Einstein temperatures, $\Theta_{\mathrm{E},11} = 85$ K and $\Theta_{\mathrm{E},22} = 64$ K, whilst for Ba1 no enhanced vibration modes were observed. Although the treatment of the temperature-dependent specific heat coincides with the Einstein temperatures obtained from the ADPs, a 1:1 correspondence between both sets of temperatures may be somehow artificial. Assuming that the smaller Einstein temperature belongs to the Ba2 sites, the cage structure around Ba2 and its elastic deformation may then give rise to a second almost localized vibration mode, $\Theta_{\mathrm{EL2}} = 84.8 \pm 2$ K.

Using Grüneisen relations, the molar specific heat c_P^{mol} can be compared to the thermal expansion on the basis of the following equation [16]:

$$\frac{\mathrm{d}L}{L}(T) = \Gamma \frac{\chi_s}{3V} \int_0^T C_P(T')\,\mathrm{d}T' = \Gamma \frac{\chi_s D}{3M} \int_0^T c_P^{\mathrm{mol}}(T')\,\mathrm{d}T' \tag{2}$$

with Γ—Grüneisen parameter, χ_S—adiabatic compressibility, C_P—heat capacity at constant pressure, V—volume, D—density, M—mass of formula unit in gram (g-atom).

For the estimation of the thermal expansion from the specific heat we assume that the temperature dependence of the Grüneisen parameter, the density and the compressibility can be neglected. Using a value of $\frac{\Gamma \chi_s D}{3M} = 6.153 \times 10^{-10}$ g-atom mJ^{-1} the thermal expansion was calculated by equation (2), and it shows fine agreement with experimental data in figure 7(b).

3.3.2. Inelastic neutron scattering. Inelastic neutron scattering (INS) can be used to probe the spectral function $F(\omega)$ directly. The evaluation of the density of states from INS data is, however, subject to perturbations due to the interaction properties of the sample constituents with neutrons. On the one hand, the effective phonon scattering cross section is proportional to the nuclear scattering cross section σ_i of atom i divided by the atomic mass M_i. On the other hand, in the case of coherent scattering contributions, the scattering process is subject to selection rules leading to a Q-dependent intensity variation. An overview on the cross sections, atomic masses and the effective inelastic scattering power of the sample constituents is given in table 5.

From the effective inelastic scattering power of the nuclei σ_i/M_i one can judge that INS is four times more sensitive to vibrations associated with the Ge and 2.5 times more sensitive to Zn modes than to the dynamics of Ba. Hence, the so-called generalized density of states $G(\omega)$ that is computed from INS data overestimates the contribution of Ge and Zn to the true spectral density $F(\omega)$. As a consequence, one has to take some care when comparing the spectral density approximated from specific heat measurements with $G(\omega)$ measured by INS.

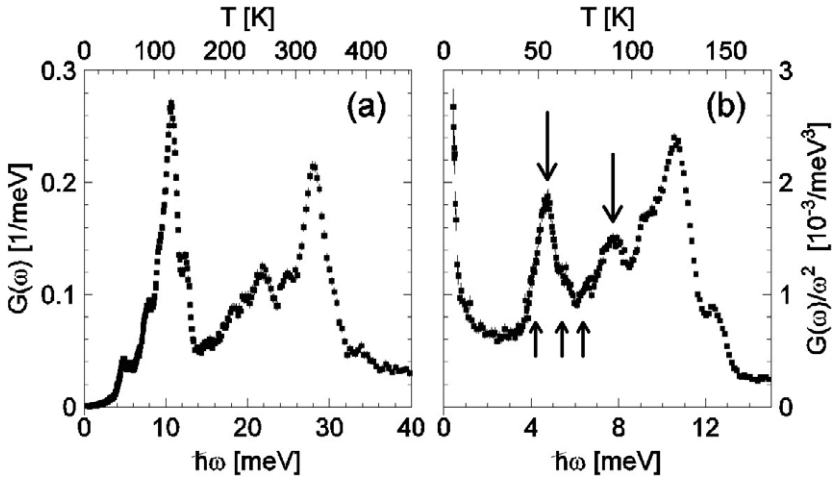

Figure 9. (a) Generalized density of states $G(\omega)$ of $Ba_8Zn_{7.7}Ge_{38.3}$ measured by time-of-flight neutron spectroscopy. (b) Low-energy region of $G(\omega)$ plotted as $G(\omega)/\omega^2$ to stress two additional modes as indicated by the vertical arrows pointing downwards. Arrows pointing upwards emphasize the substructure of the peaks, i.e. shoulders and pre-peaks.

Table 5. Coherent and incoherent cross sections, atomic masses of the sample constituents and effective inelastic cross section σ_i/M_i.

Atom	Coherent cross section (b)	Incoherent cross section (b)	amu	σ_i/M_i
Ba	3.23	0.15	137.3	0.024 62
Zn	4.05	0.08	65.4	0.063 15
Ge	8.42	0.18	72.6	0.118 46

Figure 9 reports the $G(\omega)$ computed from INS data taken at the time-of-flight spectrometer IN6 at the Institute Laue Langevin in Grenoble, France. For a clear presentation, the total of $G(\omega)$ has been normalized to three modes in the energy range up to 32 meV. The data have been collected with an incident neutron wavelength of about 0.41 nm in the extreme time-focusing mode, offering an energy resolution of 0.15 meV in the energy range up to 10 meV. $G(\omega)$ has been computed from the signal averaged over the entire Q-range accessed with the experiment. This data evaluation procedure is known as incoherent approximation.

As is indicated in figure 9(a), $G(\omega)$ is dominated by three strong intensity maxima in this range. The maxima are centred at about 10.5 meV (125 K), 22 meV (250 K) and 28 meV (325 K), respectively. We may assume that due to the stoichiometry of the sample and the effective phonon cross sections these maxima reflect mainly the dynamics of Ge atoms. For a comparison with the specific heat data it is important to focus on the energy range below 15 meV (170 K). To stress the details of the inelastic response we have chosen its presentation as $G(\omega)/\omega^2$ in figure 9(b). As has already been discussed above, the Debye theory of the solid state leads to an energy-independent constant value for $G(\omega)/\omega^2$ being related to the average velocity of sound of acoustic phonons. In realistic samples deviations from this constant value occur in terms of Einstein modes. As a general rule in simple crystals, they are due to optic phonon modes. In complex crystalline structures like the present one they are additionally supposed to be due to localized vibrations of the guests, i.e. the encaged barium atoms in the present clathrate.

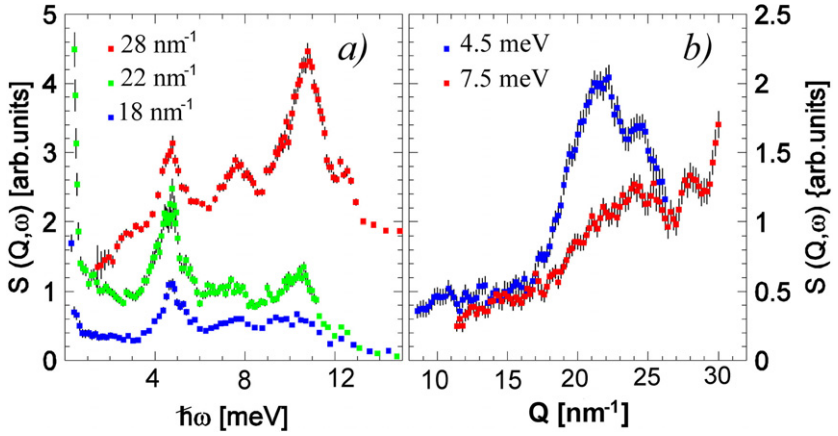

Figure 10. (a) Constant Q cuts of the dynamic structure factor $S(Q, \omega)$ of $Ba_8Zn_{7.7}Ge_{38.3}$. Q-numbers are indicated in the figure. Note that spectrum taken at 28 nm^{-1} is shifted by 15 nm^{-1} for clarity. (b) Constant-energy cuts of $S(Q, \omega)$ at energies corresponding with the positions of the two low-energy Einstein modes.

In fact, in addition to the strong peak at 11.5 meV, figure 9(b) evidences the presence of two pronounced low-energy Einstein modes centred at about 4.7 meV (55 K) and 7.7 meV (90 K). In general the mode energies correspond well with the energies of the two modes conjectured from specific heat measurements, though they are apparently shifted slightly towards higher energies. However, a closer inspection of the maxima profiles reveals a more complex line shape than might be expected for single excitations. For example, there are shoulders at 4 meV (46 K) and 5.5 meV (64 K) on the first maximum and a pre-peak at 6.5 meV (75 K) at the second maximum. This detailed response is counterintuitive for localized vibrations and points to a possible coupling of the Ba atoms with the host lattice. Such a supposed coupling requires the contribution of Ge and Zn dynamics to the identified low-energy Einstein modes.

To exemplify the effect of the predominantly coherent scattering of the sample we report in figure 10 constant Q cuts (a) and constant energy cuts (b) of the dynamic structure factor $S(Q, \omega)$ which can be well compared with $G(\omega)/\omega^2$ in figure 9(b). The non-systematic changes of intensity upon Q and energy variation are the manifestation of phonon selection rules that are governed by the symmetry of the sample. It is obvious that for coherent scatterers the details of the intensity distribution in $G(\omega)$ obtained in the incoherent approximation depend decisively on the Q-range accessed with the experiment. The effect of different Q-sampling can be best judged from figure 10(b), where a pronounced broad maximum centred around 22 nm^{-1} is detected. It is due to the average dispersion of acoustic phonons.

Nonetheless, as can be seen in figure 10(a), the presence of the two low-energy Einstein modes is well established in a wide Q-range. The 4.7 meV mode is rather the dominating feature in $S(Q, \omega)$ at low Q. At any inspected Q its line shape proves to be more structured than expected for a single excitation. This feature and the non-monotonic intensity change of the two Einstein modes upon Q-variation could be interpreted as indicators for a coupling between the Ba modes and the Zn and Ge dynamics. They are, however, in agreement with the postulation of an intrinsic width of the two Einstein modes based on the specific heat measurements and the conclusions drawn from thermal conductivity measurements presented below.

3.3.3. Optical measurements. The reflectance and the optical conductivity obtained by ellipsometry are shown in figure 11.

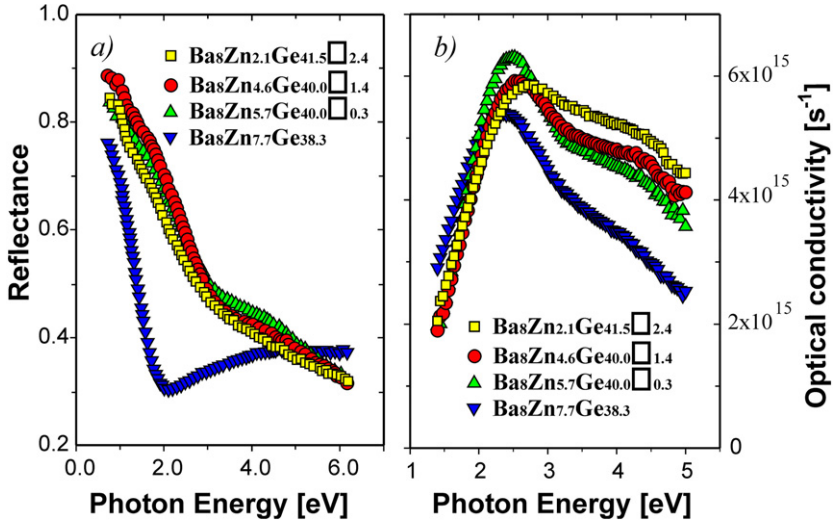

Figure 11. (a) Optical reflectance of $BaZn_xGe_{46-x-y}\square_y$, $x = 2.1, 4.6, 5.7$ and 7.7 at room temperature. (b) Optical conductivity of $BaZn_xGe_{46-x-y}\square_y$, $x = 2.1, 4.6, 5.7$ and 7.7 as obtained by spectroscopic ellipsometry at room temperature.

Table 6. Optical parameters obtained from reflectance data using the Drude model for the free carrier contribution and one Lorentz oscillator (peak energy ω_0) accounting for the interband transition.

Sample	$h^2\omega_p^2$ (eV^2)	ρ(300 K, $\omega = 0$) ($\mu\Omega$ cm)	ω_0 (eV)
$Ba_8Zn_{2.1}Ge_{41.5}\square_{2.4}$	2.2	710	0.49
$Ba_8Zn_{4.6}Ge_{40.0}\square_{1.4}$	2.4	377	0.48
$Ba_8Zn_{5.7}Ge_{40.0}\square_{0.3}$	2.9	526	0.45
$Ba_8Zn_{7.7}Ge_{38.3}$	0.62	1121	0.73

The reflectance data have been fitted using the Drude model for the frequency-dependent dielectric function; one Lorentzian oscillator has been added to the model in order to account for the interband absorption contribution.

The plasma frequency, obtained from a best-fit procedure, together with the extrapolated zero-frequency limit of the resistivity and the energy of the Lorentzian peak, is shown in table 6.

A slight increase of the plasma frequency ω_p with Zn content can be observed for samples until the nominal concentration $Ba_8Zn_{5.7}Ge_{40.0}\square_{0.3}$. Then, an abrupt change occurs and ω_p drops to a much lower value. In the simplest model, ω_p is related to the charge carrier density n and to $m^* = m/m_e$, reflecting the effective mass. m is the actual and m_e the free electron mass, i.e., $\omega_p^2 = 4\pi e^2 n/(m_e m^*)$. The ratio n/m^* in cm^{-3} follows then simply from $n/m^* = 7.2 \times 10^{20} \times \omega_p^2$ (for ω in eV). Thus, n/m^* significantly decreases, from 1.58×10^{21} to 4.46×10^{20} cm^{-3}. Since the Sommerfeld value γ of these materials keeps very small, and frequently, semimetal or semiconductors have small effective masses too, the carrier concentration n will reduce accordingly. Using the lattice constants of the present series, a decrease from 2 carriers/unit cell in $Ba_8Zn_{2.1}Ge_{41.5}\square_{2.4}$ to about 0.56 carriers/unit cell for $Ba_8Zn_{7.7}Ge_{38.3}$ follows straightforwardly. The extrapolated values for the resistivities are in general not far from the measured ones, apart from $Ba_8Zn_{2.1}Ge_{41.5}\square_{2.4}$, for which a much lower value is obtained. This possibly relates to the mechanical quality of the present series of

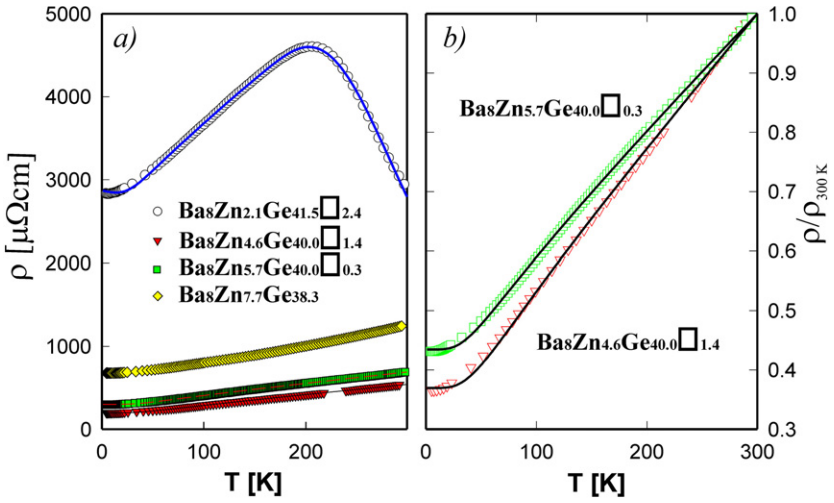

Figure 12. (a) Temperature-dependent resistivity ρ of $Ba_8Zn_xGe_{46-x-y}\square_y$. The solid line is a fit to the compound $Ba_8Zn_{2.1}Ge_{41.5}\square_{2.4}$ (see text). (b) Normalized resistivity of $Ba_8Zn_{4.6}Ge_{40.0}\square_{1.4}$ and $Ba_8Zn_{5.7}Ge_{40.0}\square_{0.3}$. The solid lines are least-squares fits according to the Bloch–Grüneisen formula.

samples, being very brittle. Optics, of course, does not use contacts; hence the brittleness is only of minor importance.

A very small decrease of the interband absorption edge seems to occur for the first three samples, but again an sudden change occurs for $Ba_8Zn_{7.7}Ge_{38.3}$. Simultaneously, a small decrease of the main absorption peak is derived from 2.73 eV ($Ba_8Zn_{2.1}Ge_{41.5}\square_{2.4}$) to 2.56 eV ($Ba_8Zn_{4.6}Ge_{40.0}\square_{1.4}$) and 2.47 eV ($Ba_8Zn_{5.7}Ge_{40.0}\square_{0.3}$), which is accompanied by an enhancement of intensity. A major change, however, occurs again for $Ba_8Zn_{7.7}Ge_{38.3}$, where the peak is at 2.35 eV with a larger extent in the infrared region.

3.3.4. Temperature-dependent electronic transport. Materials characterized by large thermopower values, being promising for thermoelectric applications, are usually found in the proximity of a metal-to-insulator transition. Hence doping and substitutions are valuable tools to reduce the charge carrier density of a certain family of compounds to an optimum level. The resistivities of such materials, however, become large, frequently behaving in between a simple metallic state and semiconducting features. Moreover, relatively small gaps Δ in the electronic density of states near the Fermi energy drive a continuous crossover from metallic-like transport to a more semiconducting-like behaviour. Such features are also obvious for the series $BaZn_xGe_{46-x-y}\square_y$, $x = 2.1$, 4.6, 5.7 and 7.7, respectively; compare figures 12(a) and (b).

While samples with larger Zn concentrations behave in a metallic manner, the $Ba_8Zn_{2.1}Ge_{41.5}\square_{2.4}$ compound obviously shows at low temperatures a metallic-like resistivity. At higher temperatures, however, there is a crossover to an activation-like dependence of $\rho(T)$. The simplest manner to describe $\rho(T)$ of metallic systems is to employ the Bloch–Grüneisen model, which considers scattering of charge carriers on thermally excited phonons. The latter are taken into account in terms of the Debye model. The phonon resistivity ρ_{ph} then reads

$$\rho_{ph} = \frac{C}{\Theta_D}\left(\frac{T}{\Theta_D}\right)^5 \int_0^{\Theta_D/T} \frac{z^5 dz}{(e^z - 1)(1 - e^{-z})} \tag{3}$$

where C is a temperature-independent electron–phonon interaction constant and Θ_D is the Debye temperature. Equation (3) causes a T^5 behaviour at low temperatures ($T \ll \Theta_D$), whilst at elevated temperatures $\rho(T)$ should behave linearly. Least-squares fits according to equation (3) (solid lines, figure 12(b)) reveal $\Theta_D = 235$ and 210 K for the $Ba_8Zn_{4.6}Ge_{40.0}\square_{1.4}$ and $Ba_8Zn_{5.7}Ge_{40.0}\square_{0.3}$ compounds, respectively. While above about 30 K the fit is convincing, at lower temperatures distinct differences between the experimental data and equation (3) occur, most likely as a consequence of the insufficient phonon model, missing a pronounced Einstein-like contribution. A description of $\rho(T)$ of the $Ba_8Zn_{7.7}Ge_{38.3}$ sample in terms of equation (3) totally fails since the data exhibit a positive slope, i.e., $d\rho/dT > 1$; such behaviour can never be traced by equation (3).

The $Ba_8Zn_{2.1}Ge_{41.5}\square_{2.4}$ sample, however, shows low-temperature behaviour reminiscent of metals, whilst at higher temperatures an activation-type resistivity becomes evident. In order to account for such distinct features, we have developed a model [15], combining the description of simple metals via the Bloch–Grüneisen law with a temperature-dependent charge carrier density. The most basic assumptions are an electronic density of states (DOS) represented by a rectangular band and a gap Δ right above the Fermi energy. The charge carrier density is then calculated via standard statistics considering the Fermi–Dirac distribution function [1, 15]. A least-squares fit according to this procedure is shown in figure 12(a) as a solid line. The principal parameter is the gap width Δ, derived as 1650 K. Although the applied model is quite simple, it fairly well describes the temperature-dependent resistivity of $Ba_8Zn_{2.1}Ge_{41.5}\square_{2.4}$. The metallic behaviour derives from scattering of conduction electrons into unoccupied sites in reciprocal space just above the Fermi energy. Once this region of the DOS becomes occupied, electrons have to be promoted across the gap, originating in semiconducting features. However, a distinct exponential behaviour does not become obvious due to the proximity to the metallic state.

The temperature-dependent thermal conductivity, λ, of $Ba_8Zn_xGe_{46-x-y}\square_y$ is displayed in figure 13(a) for a temperature range from 4 K to room temperature. The main characteristics of all the samples measured are pronounced maxima at low temperatures. This feature is opposite to a number of clathrates, e.g. $Eu_8Ga_{16}Ge_{30}$ [17], where $\lambda(T)$ does not exhibit a maximum in this temperature range. The suppression of these kinds of maxima is attributed to *resonance scattering* as demonstrated recently by Nolas *et al* [18]. This scattering of the heat-carrying phonons is based on static and dynamic disorder associated with the *rattling* motion of the guest atoms, i.e. Ba2, in the large voids of the structure formed by Zn and Ge. In general, this mechanism has a large impact on thermal transport and is considered responsible for the glass-like transport in cage-forming compounds such as clathrates and skutterudites. In comparison to already mentioned $Eu_8Ga_{16}Ge_{30}$, the Zn-based compounds have overall larger thermal conductivities. In a basic theory of thermal conductivity, the atomic masses distinctly influence the absolute values of $\lambda(T)$. The heavier the masses involved, the lower overall $\lambda(T)$. Thus the smaller masses of Zn/Ga and Ba/Eu straightforwardly explain the higher $\lambda(T)$ values observed in $Ba_8Zn_xGe_{46-x-y}\square_y$. An approximation according to Cahill and Pohl [19] allows us to estimate the theoretical lower limit of the lattice thermal conductivity which primarily is defined by the number of atoms per unit volume and by the Debye temperature. Taking $n = 4.32 \times 10^{28}$ m^{-3} and $\theta_D = 225$ K for $Ba_8Zn_{7.7}Ge_{38.3}$ reveals $\lambda_{min}(300\ \text{K}) = 4.3$ mW cm^{-1} K^{-1}. Results below room temperature are shown in figure 13(a).

A more quantitative description of $\lambda(T)$ is possible in terms of Callaway's theory of lattice thermal conductivity λ_ℓ. To derive λ_ℓ from the total thermal conductivity λ, the Wiedemann–Franz law is applied to $\rho(T)$ data, allowing us to define λ_e. Although the Wiedemann–Franz law is valid in extended temperature ranges only for free electron systems, it is widely used even for complex materials such as skutterudites or clathrates. The Wiedemann–Franz

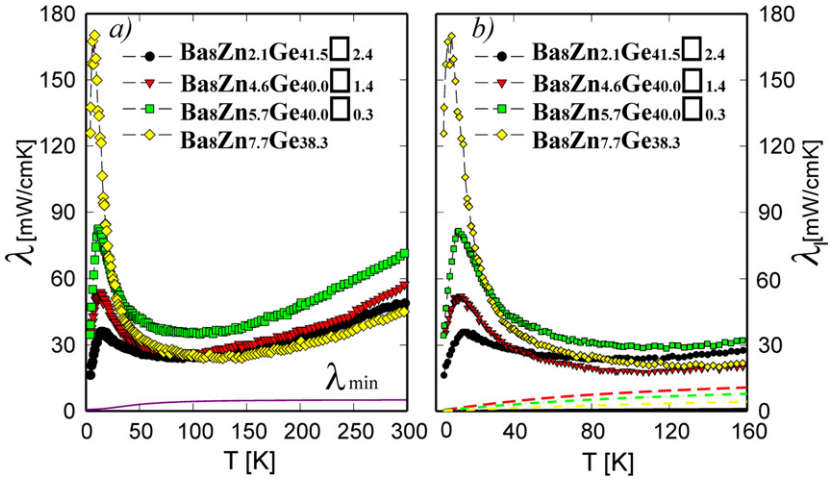

Figure 13. (a) Temperature-dependent thermal conductivity λ of $Ba_8Zn_xGe_{46-x-y}\square_y$ with $x = 2.1, 4.6, 5.7, 7.7$. The hatched area renders the minimum thermal conductivity (see text). (b) Lattice thermal conductivity λ_ℓ of $Ba_8Zn_xGe_{46-x-y}\square_y$ (small symbols) and electronic contribution λ_e (dashed lines).

relation states that increasing electrical resistivities cause decreasing λ_e values. If, for example, $\rho(295\ \mathrm{K}) = 720\ \mu\Omega$ cm, $\lambda_e = 10$ mW cm^{-1} K^{-1}; a resistivity of 100 $\mu\Omega$ cm is equivalent to 72 mW cm^{-1} K^{-1}. The relatively large resistivities of the series investigated cause λ_e values well below λ_ℓ, (dashed lines, figure 13(b)). The temperature dependence of λ_ℓ follows from the basic thermodynamic expression $\lambda = (1/3) \cdot C_V \cdot v \cdot l$, where C_V is the heat capacity of the system, v the particle velocity and l the mean free path. According to Callaway [20], this transforms for the heat-carrying lattice vibrations to

$$\lambda_\ell = CT^3 \int_0^{\theta_D/T} \frac{\tau_c x^4 \exp(x)}{[\exp(x) - 1]^2}\, dx \tag{4}$$

where τ_c represents the overall relaxation time for scattering processes; C is a constant and θ_D is the Debye temperature.

Taking into account the most relevant scattering processes present in the clathrates investigated, the relaxation time can be expressed as

$$\tau_c^{-1} = \tau_B^{-1} + \tau_D^{-1} + \tau_U^{-1} + \tau_E^{-1} \tag{5}$$

where the subscripts B, D, U, and E refer to scattering processes of the heat-carrying phonons with boundaries, point defects, Umklapp processes and scattering on electrons, respectively. Equation (5) does not contain terms for resonance scattering, since they seem to be of minor importance in the series of compounds studied. Additionally, a T^3 term was added to equation (4) in order to get rid of radiation losses, proprietary to the steady state heat flow method used. Equation (4) highlights that the lattice thermal conductivity can be strongly influenced by scattering on the charge carrier system, too ($\tau_E^{-1} = E\omega$, E is a material constant). This seems to significantly influence λ_ℓ at somewhat elevated temperatures. The compound having the lowest electrical resistivity, and thus the largest charge carrier density, i.e., $Ba_8Zn_{4.6}Ge_{40.0}\square_{1.4}$, exhibits a well-reduced lattice thermal conductivity above about 100 K. On the other hand, the lattice thermal conductivity of $Ba_8Zn_{2.1}Ge_{41.5}\square_{2.4}$ becomes much larger, most likely due to the reduced efficiency of phonon scattering on conduction

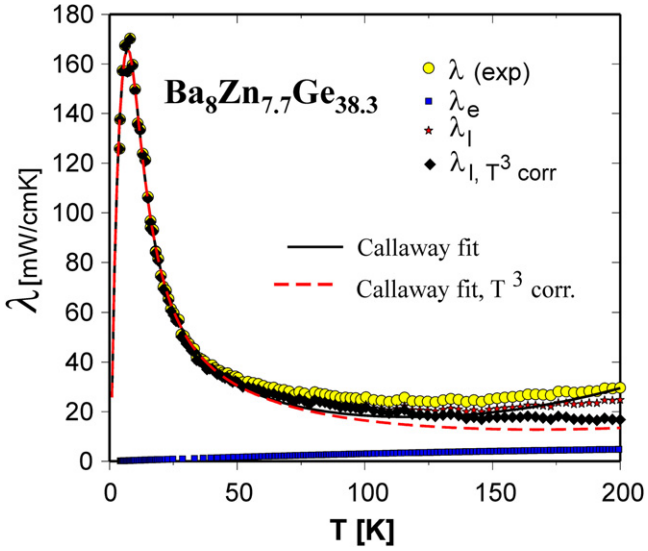

Figure 14. Temperature-dependent thermal conductivity λ of $Ba_8Zn_{7.7}Ge_{38.3}$ (large circles). The electronic λ_e (filled small squares) and the lattice contribution λ_ℓ (filled small stars) are derived from the Wiedemann–Franz law. The small diamonds represent the lattice contribution corrected for radiation losses. The solid and the dashed lines are least-squares fits applying the model of Callaway with and without a T^3 term for radiation losses.

electrons. As indicated above, this compound is next to a metal-to-insulator transition. A further interesting feature is the observation that the low-temperature maximum in $\lambda(T)$ of the present series becomes more pronounced with increasing Zn content and reaches its maximum for the $Ba_8Zn_{7.7}Ge_{38.3}$-based compound. Although this sequence is expected to introduce some disorder in the crystal structure, and thus enhances the thermal resistivity, the vanishing of the vacancies in the lattice due to the Zn/Ge substitution, which obviously completes for the $Ba_8Zn_{7.7}Ge_{38.3}$ compound (compare figure 1), seems to overcompensate by far the former mechanism.

Results of least-squares fits according to equation (4) and (5) are shown as solid and dashed lines in figure 14 for $Ba_8Zn_{7.7}Ge_{38.3}$. The dashed line corresponds to the T^3 correction and demonstrates that the lattice thermal conductivity of this compound is in proximity of the theoretical limit of thermal conductivity, a necessity for thermoelectric applications of these materials. The initial rise of $\lambda_\ell(T)$ may be referred to boundary and point defect scattering; it becomes large when both quantities are small. Note that defects also comprise vacancies. If the strength of Umklapp scattering increases, $\lambda_\ell(T)$ starts to strongly decrease above a certain temperature, thereby forming a maximum at lower temperatures. The latter weakly depends on the Debye temperature but occurs well below $\Theta_D/10$. Additionally, an increase of Θ_D slightly reduces overall $\lambda_\ell(T)$ values.

Measurements of the temperature-dependent thermopower are shown in figure 15 for $Ba_8Zn_x(Ge_{46-x-y}\square_y)$. Common to all systems displayed are negative $S(T)$ values, referring to electrons as majority charge carriers.

Moreover, $S(T)$ exhibits weak low-temperature structures as a consequence of phonon-drag effects. The compound richest in Zn, however, behaves almost linearly up to the 600 K range (inset, figure 15). Deviations from linearity are most likely measurement errors. $Ba_8Zn_{7.7}Ge_{38.3}$ is characterized by a slope of $-0.28\ \mu V\ K^{-2}$. Linearity of the diffusion

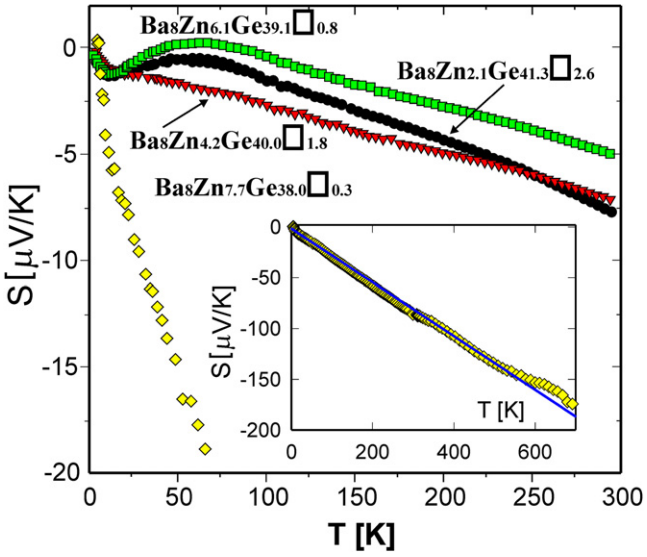

Figure 15. Temperature-dependent thermopower of $Ba_8Zn_xGe_{46-x-y}\square_y$ with $x = 2.1$, 4.6, 5.7, 7.7.

thermopower is predicted in terms of the free-electron model [21]. For $T > \theta_D$, electron–phonon interaction dominates.

$$S_d(T > \Theta_D) = \frac{\pi^2 k_B^2 2m}{e\hbar^2(3n\pi^2)^{2/3}}T. \tag{6}$$

This simple relation allows an estimation of the charge carrier densities. Taking $m = m_e$, which should hold at high temperatures for systems without significant electronic correlations, the charge carrier density is estimated to be $n \approx 6 \times 10^{20}$ cm^{-3}, in excellent agreement with the optical data. These numbers appear reasonable in comparison to e.g. Ba_6Ge_{25} [21], where a charge carrier density $n \approx 7.8 \times 10^{21}$ cm^{-3} was observed from Hall data; the Seebeck effect for that compound is about 10 times smaller than that of $Ba_8Zn_{7.7}Ge_{38.3}$.

4. Summary

Starting from binary $Ba_8Ge_{43}\square_3$, a series of clathrates was synthesized forming a solid solution, $Ba_8Zn_x(Ge_{46-x-y}\square_y)$, with a solubility limit of 8 Zn atoms per formula unit at 800 °C. Throughout the homogeneity region cubic primitive symmetry consistent with the space group type $Pm\bar{3}n$ as typical for clathrate type I has been confirmed. Phase relations were derived at subsolidus temperatures as well as at 800 °C. Physical properties, such as charge carrier density and transport quantities, were found to be heavily influenced by Ge/Zn substitution in the clathrate framework: the system is driven towards a metal-to-insulator transition, as is obvious from the temperature-dependent resistivity of $Ba_8Zn_xGe_{46-x-y}\square_y$ for $2.1 \leqslant x \leqslant 7.7$. These qualitative arguments are corroborated from the derived plasma frequencies, indicating a decrease of the charge carrier density from about 10^{21} to 10^{20} cm^{-3}, as one proceeds from $x_{Zn} = 2.1$ to 7.7. Besides the charge carrier density, also the carrier mobility changes throughout the series, being much higher for the nominal $x_{Zn} = 7.7$ system; consequently, the overall resistivity is even below that of the system with nominal $x_{Zn} = 5.7$. Such a behaviour can possibly be correlated to the vanishing of the voids in the crystal structure as already noted in the

context of the temperature-dependent thermal conductivity. A model of the electronic density of states, characterized by a narrow gap right above the Fermi energy, allowed us to qualitatively define details of the temperature-dependent electrical resistivity. Thermal conductivity data are modelled in terms of Callaway's theory of heat-carrying phonons. Moreover, phonons have been studied by INS, C_p and thermal expansion experiments identifying low-energy optical modes, which are characterized by a correlated movement of the Ba2 filler and the Zn/Ge framework atoms. Measurements of the Seebeck coefficient allowed testing these materials with respect to their thermoelectric performance. For $Ba_8Zn_{7.7}Ge_{38.3}$ a figure of merit $ZT = S^2T/(\rho\lambda) \approx 0.035$ is derived at room temperature from the present experimental data. This value, however, neglects the correction of radiation losses, which, when applied, renders ZT_{corr} (300 K) $= 0.087$. Using the experimental thermopower data at 700 K together with careful extrapolations of resistivity (ρ(700 K) $\approx$ 2150 $\mu\Omega$ cm) and of thermal conductivity (λ_{corr}(700 K) $\approx$ 25 mW cm^{-1}K^{-1}) we obtain ZT_{corr}(700 K) $= 0.42$. Applications are possible, if the thermoelectric figure of merit approaches a value of $ZT \approx 1$, as realized in Bi_2Te_3 with ZT(300 K) ≈ 0.7 [22]. Fine-tuning of the charge carrier concentration is in progress to drive this class of materials to even more promising values of the thermoelectric efficiency.

Acknowledgments

The research reported herein was supported by the Austrian FWF projects P16370, P19165 and P16778-No2. NM-K and PR are both grateful to the OEAD Austrian–Ukrainian Scientific-Technological Exchange Program 'Ernst Mach' for fellowships in Vienna.

References

[1] Melnychenko-Koblyuk N, Grytsiv A, Berger St, Kaldarar H, Michor H, Röhrbacher F, Royanian E, Bauer E, Rogl P, Schmid H and Giester G 2007 *J. Phys.: Condens. Matter* **19** 046203
[2] Czybulka A, Kuhl B and Schuster H U 1991 *Z. Anorg. Allg. Chem.* **594** 23
[3] Kuhl B, Czybulka A and Schuster H U 1995 *Z. Anorg. Allg. Chem.* **621** 1
[4] Carrillo-Cabrera W, Borrmann H, Paschen S, Baenitz M, Steglich F and Grin Y 2005 *J. Solid State Chem.* **178** 715
[5] Carrillo-Cabrera W, Curda J, Petters K, Baenitz M, Grin Y and Schnering V H G 2000 *Z. Kristallogr. New Cryst. Struct.* **215** 321
[6] Carrillo-Cabrera W, Budnyk S, Prots Y and Grin Y 2004 *Z. Anorg. Allg. Chem.* **630** 7226
[7] Rotter M, Müller H, Gratz E, Doerr M and Loewenhaupt M 1998 *Rev. Sci. Instrum.* **69** 2742
[8] Chernyavsky O, Prokes K, Sechovsky V, Doerr M, Rotter M and Loewenhaupt M 2002 *Czech. J. Phys.* **52** A237
[9] Rotter M, Lindbaum A, Doerr M, Loewenhaupt M, Müller H, Jobiliong E and Brooks J 2005 *Phys. Rev.* B **72** 52404
[10] Parthé E, Gelato L, Chabot B, Penzo M, Cenzual K and Gladyshevskii R 1994 *TYPIX Standardized Data and Crystal Chemical Characterization of Inorganic Structure Types* (Berlin: Springer)
[11] Qiu L, Swainson I P, Nolas G S and White M A 2004 *Phys. Rev.* B **70** 035208
[12] Willis B T M and Pryor A W 1975 *Thermal Vibrations in Crystallography* (Cambridge: Cambridge University Press)
[13] Junod A, Bichsel D and Mueller J 1979 *Helv. Phys. Acta* **52** 580
[14] Junod A, Jarlborg T and Mueller J 1983 *Phys. Rev.* B **27** 1568
[15] Berger St 2003 *PhD Thesis* Vienna University of Technology
[16] Barron T, Collins J and White G 1980 *Adv. Phys.* **29** 609
[17] Cohn J L, Nolas G S, Fessatidis V, Metcalf T H and Slack G A 1999 *Phys. Rev. Lett.* **82** 779
[18] Nolas G, Cohn J L, Slack G and Schujman S B 1998 *Appl. Phys. Lett.* **73** 178
[19] Cahill D G and Pohl R O 1989 *Solid State Commun.* **70** 927
[20] Callaway J and Baeyer H C 1960 *Phys. Rev.* **120** 1149
[21] Paschen S, Tran V H, Baenitz M, Carrillo-Cabrera W, Grin Y and Steglich F 2002 *Phys. Rev.* B **65** 134435
[22] Tritt T 1999 *Science* **283** 804